Joule

CellPress
OPEN ACCESS

Article

Structural changes in the silver-carbon composite anode interlayer of solid-state batteries

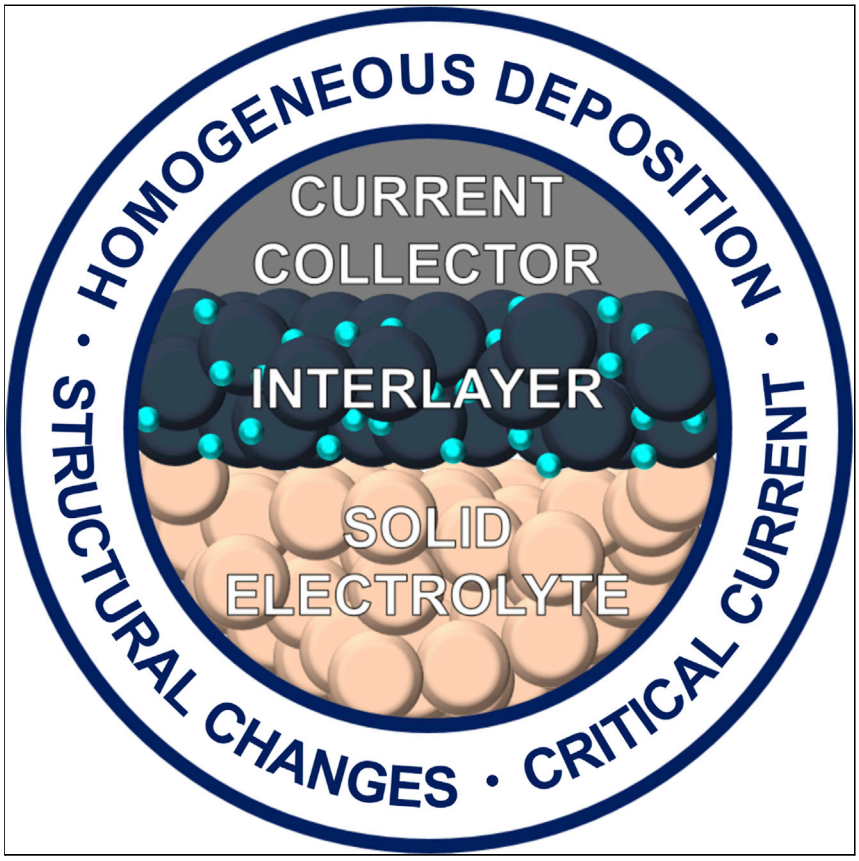

Anodeless solid-state batteries have the potential to increase the energy density and safety of batteries, but they face challenges, including inhomogeneous plating of Li metal on the current collector and penetration of Li metal dendrites into the solid electrolyte. Introduction of an Ag-C composite interlayer between the solid electrolyte and current collector mitigates these problems. Here, we study the structural changes within the composite interlayer, the critical current density, and the morphology of the deposited Li/Ag.

Dominic Spencer-Jolly, Varnika Agarwal, Christopher Doerrer, ..., Patrick S. Grant, Robert A. House, Peter G. Bruce

peter.bruce@materials.ox.ac.uk

Highlights

Operando XRD reveals structural changes in Ag-C interlayer during cycling

Ag nanoparticles do not increase critical current of graphite-based interlayer

The role of Ag nanoparticles is to facilitate homogeneous Li and Li-Ag deposition

Spencer-Jolly et al., Joule 7, 503–514
March 15, 2023
https://doi.org/10.1016/j.joule.2023.02.001

Joule

CellPress
OPEN ACCESS

Article

Structural changes in the silver-carbon composite anode interlayer of solid-state batteries

Dominic Spencer-Jolly,[1,3] Varnika Agarwal,[1,3] Christopher Doerrer,[1] Bingkun Hu,[1] Shengming Zhang,[1] Dominic L.R. Melvin,[1] Hui Gao,[1] Xiangwen Gao,[1] Paul Adamson,[1] Oxana V. Magdysyuk,[2] Patrick S. Grant,[1] Robert A. House,[1] and Peter G. Bruce[1,4,*]

SUMMARY

Ag-carbon composite interlayers have been reported to enable Li-free (anodeless) cycling of solid-state batteries. Here, we report structural changes in the Ag-graphite interlayer, showing that on charge, Li intercalates electrochemically into graphite, subsequently reacting chemically with Ag to form Li-Ag alloys. Discharge is not the reverse of charge but rather passes through Li-deficient Li-Ag phases. At higher charging rates, Li intercalation into graphite outpaces the chemical reactions with Ag, delaying the formation of the Li-Ag phases and resulting in more Li metal deposition at the current collector. At and above 2.5 mA·cm^{-2}, Li dendrites are not suppressed. Ag nanoparticles do not suppress dendrites more effectively than does an interlayer of graphite alone. Instead, Ag in the carbon interlayer results in more homogeneous Li and Li-Ag formation on the current collector during charge.

INTRODUCTION

Solid-state batteries containing a Li anode and a ceramic electrolyte offer a possible route to higher energy density and increased safety, compared with liquid electrolyte Li-ion batteries.[1,2] Charging at practical rates can lead to the formation of Li dendrites (filaments) at the anode that penetrate the ceramic electrolyte, leading to short circuit and cell failures.[3,4] Furthermore, forming solid-state cells free from Li metal initially (so-called anodeless cells) are attractive but come with problems, including inhomogeneous Li distribution, which can compromise cycling.[5]

In an effort to circumvent the problem of Li dendrites, thin layers of a wide range of materials have been deposited on the solid electrolyte surface at the anode.[6–10] On charging, the layer forms an alloy with Li, rather than nucleating Li metal. Examples of layers include Mg, Al, Ge, In, Si, Sb, Sn, Au, and Ag.[11–22] Unfortunately, formation of such alloys often involves considerable volume change, leading to strain and detachment at the interface with the solid electrolyte.[23–25] Graphite, and related carbons, can intercalate Li with a relatively small volume change, typically ~10%; such layers have been studied in solid-state cells.[26–31] Recently, Lee and co-workers at Samsung reported excellent performance of an anodeless solid-state battery, using a carbon layer containing Ag nanoparticles, which results in the formation of a Li-alloy between the carbon layer and current collector on charge, the cell exhibiting in excess of 1,000 cycles at 3.2 mA·cm^{-2}.[32] In order to understand how Ag-C composite layers function, it is important to determine the structural changes that occur during cell operation.

CONTEXT & SCALE

Enabling all-solid-state batteries based on ceramic electrolytes and a Li anode could lead to increased energy storage and safer batteries. Dendrites (filaments) of Li penetrate the ceramic on charging at practical rates. Furthermore, plating Li where none is already present (anodeless cells) is desirable but difficult. Interlayers at the anode have been proposed to address these problems. Recently, promising performance was reported by Samsung Advanced Institute of Technology for a composite layer of carbon with Ag nanoparticles. Here, we explore the structural changes that occur in an Ag-graphite composite interlayer. Charging involves electrochemical Li intercalation into the graphite, then lithiated graphite reacts with Ag to form a series of Li-Ag alloys. Li-Ag and Li deposit between the interlayer and the current collector. Ag does not increase the maximum charging current before Li dendrites form, but it does lead to a more homogeneous Li-rich layer at the current collector.

Here, we employ *operando* powder X-ray diffraction (PXRD), scanning electron microscopy (SEM), and energy dispersive X-ray spectroscopy (EDX) to follow the structural changes in an Ag-graphite composite interlayer as a Li-free (anodeless) cell is charged then discharged. Graphite is chosen because diffraction can follow the structural changes upon lithiation, because graphite alone has been used as an interlayer, and because the Ag-graphite composite can facilitate Li-Ag alloy and Li metal formation on the current collector.[29] On charging, Li is intercalated electrochemically into graphite. The lithiated graphite then reacts chemically with Ag to form a series of increasingly Li-rich Li-Ag alloy phases. At higher charging rates, Li intercalation into graphite is faster than the chemical reaction with Ag, resulting in more Li-deficient Ag alloys persisting to higher states of charge (higher charge capacities). Discharge is not the reverse of charge, with other Li-Ag phases forming that are not apparent on charge. Discharge commences with electrochemical deintercalation of LiC_6, which then induces chemical dealloying with the Li chemically intercalating into LiC_x. The Ag-graphite interlayer is little or no better at suppressing dendrites than graphite alone. Dendrite resistance is determined by the rate of Li intercalation into the graphite. Carbons with higher Li diffusivity are expected to enable higher charging rates in carbon-based composite interlayers. The benefit of the composite interlayer lies in the more homogeneous deposition of Li (with no detectable Ag alloying) and Li-Ag between the interlayer and the current collector, which is more effectively stripped on discharge. This fundamental understanding of the Ag-graphite composite layer provides a path toward the design of interlayers that enable improved solid-state battery performance, with implications not only for the Ag-graphite composite layer but also for carbon-based interlayers more widely.

RESULTS AND DISCUSSION

The *operando* PXRD anodeless cell is composed of an Ag-graphite interlayer and Li_6PS_5Cl electrolyte, which was chosen as it is a strong candidate electrolyte for solid-state batteries, with a high ionic conductivity.[33,34] The composite layer is 5.7% by volume Ag, similar to that used by Lee et al.[32] The second electrode is Li metal. The Ag-graphite layer is adjacent to an Al-coated Be window, from which it is separated from the Ag-graphite layer by a thin Cu foil. The PXRD data were collected in reflection through the Be window. Details of the cell construction and *operando* experiment are given in the experimental procedures. The capacity passed on charge exceeds the capacity that can be accommodated by lithiation of the 5-μm-thick interlayer throughout this work.

Low-rate charging

A rate of 30 $\mu A \cdot cm^{-2}$ was employed to explore the structural changes at low rates of Li intercalation. Results at high rates are discussed later. The *operando* PXRD on slow charging are shown along with the load curve in Figure 1. The behavior is divided into two regions. On initial intercalation there is no change in the powder diffraction patterns, during which the potential drops to around 0.4 V. These observations are in accord with the reduction of sulfide electrolytes, as has been reported previously for graphite-only anodes.[35,36] In the second region of the load curve, the graphite peaks shift to lower two theta (e.g., the 003 peak at 26.6°) as the graphite expands during Li intercalation. At the same time, the Ag peaks at, for example, 38.3° and 44.1° shift to lower two theta, indicative of an expansion as Li forms a solid solution alloy with Ag, Li_xAg. As Ag occupies only 5.7% of the interlayer volume, there is very little direct contact between Ag and the Li_6PS_5Cl electrolyte, and direct electrochemical alloying of Ag is not expected to any significant extent. The load curve resembles that of graphite but with the capacity stretched,

[1]University of Oxford, Oxford OX1 3PH, UK
[2]Diamond Light Source, Didcot OX11 0DE, UK
[3]These authors contributed equally
[4]Lead contact
*Correspondence: peter.bruce@materials.ox.ac.uk
https://doi.org/10.1016/j.joule.2023.02.001

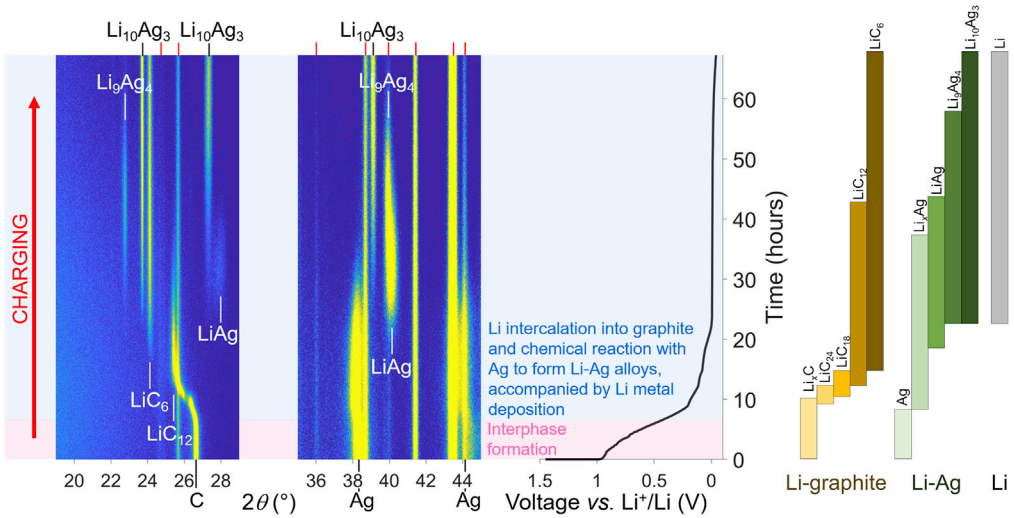

Figure 1. *Operando* powder X-ray diffraction patterns collected on charging an Ag-graphite composite layer at the anode of a cell with Li_6PS_5Cl electrolyte at a current density of 30 $\mu A \cdot cm^{-2}$

Regions of PXRD where peaks occur are shown on the left, with yellow indicating intensity. Diffraction peaks corresponding to the cell body and Li_6PS_5Cl are indicated with red marks. The center-right panel shows the corresponding charging profile vs. a Li^+/Li counter electrode. The pink background indicates the region of interphase formation, and the blue background indicates the region of Li intercalation into graphite and chemical reactivity with Ag to form Li-Ag alloys, accompanied by Li metal deposition. The far right shows a visual key indicating the phase behavior of Li-graphite (gold), Li-Ag (green), and Li metal (gray).

as discussed below. There are no voltage features indicative of electrochemical alloying of Ag (Figure S1). This is consistent with the electrochemical intercalation of Li into graphite, and the LiC_x reacting chemically with Ag, and not with the direct electrochemical alloying of Ag with Li. The net effect is that the graphite load curve is stretched in capacity due to reaction of the LiC_x with Ag. As Li is electrochemically intercalated into graphite, the chemical potential of LiC_x increases and drives the chemical reaction with Li_xAg. These observations are supported by the chemical reactivity between various Li-intercalated graphites and Ag, as discussed later. On further charging, the voltage drops to a plateau at around 105 mV and peaks appear, for example, at 25.5° two theta, corresponding to the formation of LiC_{12}. The lithiated graphite continues to react with Ag, seen by shifts in the Ag peaks. Further charging results in the formation of the fully lithiated LiC_6 phase, at which point the Li_xAg solid solution gives way to LiAg. At yet higher states of charge, LiAg transforms to Li_9Ag_4 and then finally to $Li_{10}Ag_3$, with phases coexisting over a significant portion of the charging curve. At the end of charge, only $Li_{10}Ag_3$ and LiC_6 are observed in Figure 1.[37] However, the quantity of charge passed exceeds the capacity of graphite and the Ag alloys, implying the formation of Li metal. Li is a weak X-ray scatterer, and the *operando* PXRDs are collected through a Be window. Careful analysis of the powder patterns in the capacity range where Li is expected does show evidence of Li metal (Figure S2A). Furthermore, SEM/EDX analysis indicates the presence of two types of particles emerging from the interlayer in the space between it and the current collector: those containing significant Ag are attributed to Li-Ag alloy and those with no detectable evidence of Ag indicative of Li metal. It is of course possible that these particles contain a very small amount of Ag, but given that Ag cannot be detected, we refer to them as Li metal throughout (Figure S2B).

Chemical reactivity between LiC_x and Ag

Li-intercalated graphite phases with the compositions LiC_{24}, LiC_{18}, LiC_{12}, and LiC_6 were prepared in liquid electrolyte cells, from which they were removed, washed, dried, mixed with Ag nanoparticles, pressed into disks, and the reactions monitored

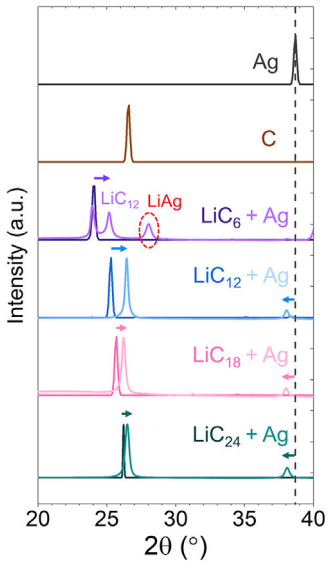

Figure 2. Powder X-ray diffraction patterns showing chemical reaction between lithiated graphite phases and Ag

Darker colors show the lithiated graphite phases before reaction with Ag; LiC_{24} (dark teal), LiC_{18} (dark pink), LiC_{12} (dark blue), and LiC_6 (dark purple). Lighter colors show the result of mixing lithiated graphite phases with Ag nanoparticles; LiC_{24} + Ag (light teal), LiC_{18} + Ag (light pink), LiC_{12} + Ag (light blue), and LiC_6 + Ag (light purple).

by PXRD. The results are shown in Figure 2. In each of the cases of LiC_{24}, LiC_{18}, and LiC_{12}, the lithiated graphite reacts with Ag, as indicated by the shift in the LiC_x peaks toward higher angles and therefore lower Li content. In the case of LiC_6, it reacts with Ag to form the LiAg phase, with LiC_6 delithiating as it does so. The LiC_x:Ag ratio was chosen in all cases such that there was sufficient (excess of) Li to react all the way to LiAg should the thermodynamic driving force of LiC_x be sufficient to do so. Only LiC_6 has a sufficiently high chemical potential (low voltage) to form LiAg. The variation of voltage with Li content for graphite and Ag is known from electrochemical cells with liquid electrolytes. Results here are in accord with these load curves, which show that only the fully lithiated LiC_6 has a voltage sufficiently low to react with Ag to form LiAg.[38–40]

Low-rate discharge

The structural changes on discharge are not simply the reverse of those on charge (Figure 3). Initially, there is relatively little change in either of the two phases $Li_{10}Ag_3$ or LiC_6. As discharging proceeds, the peaks for $Li_{10}Ag_3$, at 27.4° and 39.1° in two theta, move to higher angles consistent with volume contraction, indicating that the $Li_{10}Ag_3$ is exhibiting Li deficiency, $Li_{10-x}Ag_3$. These changes, coupled with no change in the peaks for LiC_6, suggest that as Li is electrochemically extracted from LiC_6, it reacts sufficiently rapidly with the Li and $Li_{10}Ag_3$ at the current collector to retain LiC_6. Further discharge involves disappearance of the $Li_{10-x}Ag_3$ phase as it gives way to Li_9Ag_4, while LiC_6 diminishes to be replaced by LiC_{12} as Li is deintercalated from LiC_6. At this point, the LiAg phase appears. As discharge proceeds further, Li deintercalates from LiC_{12} reforming graphite, while LiAg undergoes a phase transition from the CsCl to the UPb structure.[41] The latter is more stable than the former when it is Li deficient, and it is likely that this explains why this structural form only appears on discharge.[41] Finally, at the end of discharge, only graphite and Ag are observed.

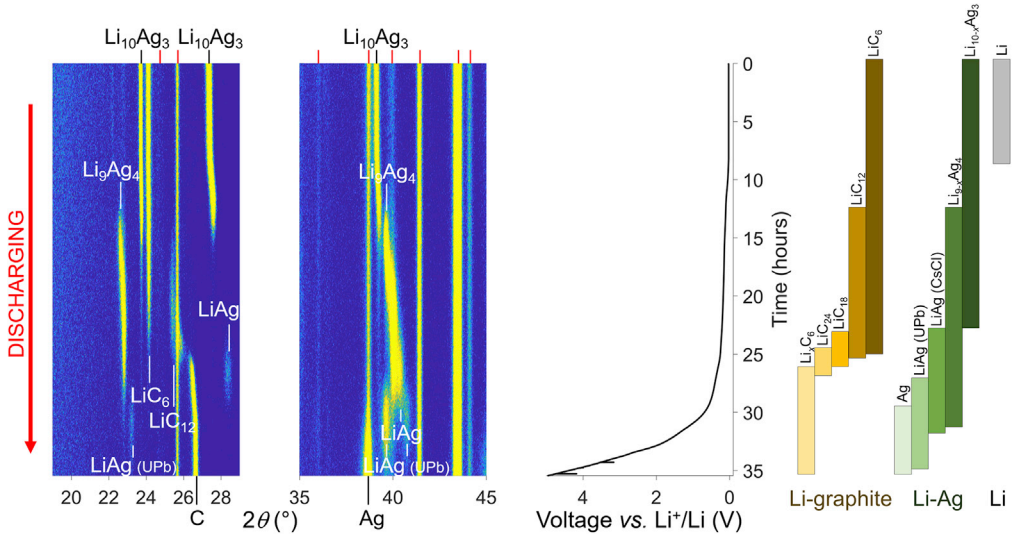

Figure 3. *Operando* powder X-ray diffraction patterns during discharge of an Ag-graphite composite layer cell carried out at a current density of 30 μA·cm^{-2}

Regions of PXRD where peaks occur are shown on the left, with yellow indicating intensity. Diffraction peaks corresponding to the cell body and Li_6PS_5Cl are indicated with red marks. The center-right panel shows the corresponding charging profile vs. a Li^+/Li counter electrode. The far right shows a visual key indicating the phase behavior of Li-graphite (gold), Li-Ag (green), and Li metal (gray).

Higher-rate charging

While data at low rates are useful in exploring the range of Li-Ag alloys that can form, it is instructive to examine the structural changes at more practical rates of 2 and 4 mA·cm^{-2} (Figure 4). As in previous work by Lee et al., cells were cycled at 60°C at these higher rates, otherwise polarization becomes severe.[32] On charging, Li intercalates into graphite, resulting in a shift of the graphite peaks to lower two theta as the lattice expands. No change is evident in the Ag peaks, indicating that the rapid insertion of Li into graphite at these rates is significantly faster than the reaction of lithiated graphite with the Ag nanoparticles. As charging proceeds, LiC_6 forms. In the case of the high rate 4 mA·cm^{-2}, LiC_x $x < 6$ persists for a higher capacity before LiC_6 forms. In the case of the data at 2 mA·cm^{-2}, once LiC_6 has been formed, Ag is replaced increasingly by LiAg and then later by $Li_{10}Ag_3$. There is also some evidence for the formation of Li_9Ag_4 peak at 39.8°, although it is heavily overlapped, as are the other Li_9Ag_4 peaks with the peaks form the cell body. At the high rate of 4 mA·cm^{-2}, there is some evidence for the formation of LiAg, although there is clear evidence of Ag persisting throughout charging. At both rates, Li metal forms.

The application of layers to the surface of solid electrolytes at the anode is motivated by the need to suppress Li metal dendrite formation and more generally to achieve efficient Li cycling in anodeless cells.[32,42] The load curve for charging at 4 mA·cm^{-2} shows a short circuit indicative of Li metal and dendrites forming electrochemically at the solid electrolyte surface. In other words, at this rate of charging, intercalation into graphite is not sufficiently fast, compared with Li metal dendrite formation, and the layer plays no useful mitigating role at 4 mA·cm^{-2} (Figure S3). We have also explored charging at 2.5 mA·cm^{-2}, and this shows a short circuit, indicating that the maximum current density that avoids Li dendrites is <2.5 mA·cm^{-2} (Figure 5A).

Graphite alone and Ag-graphite composite layers were observed to have the same failure point (Figure 5), with each observed to charge stably at 2 mA·cm^{-2} but fail due to dendrite penetration through the solid electrolyte at 2.5 mA·cm^{-2}. Based

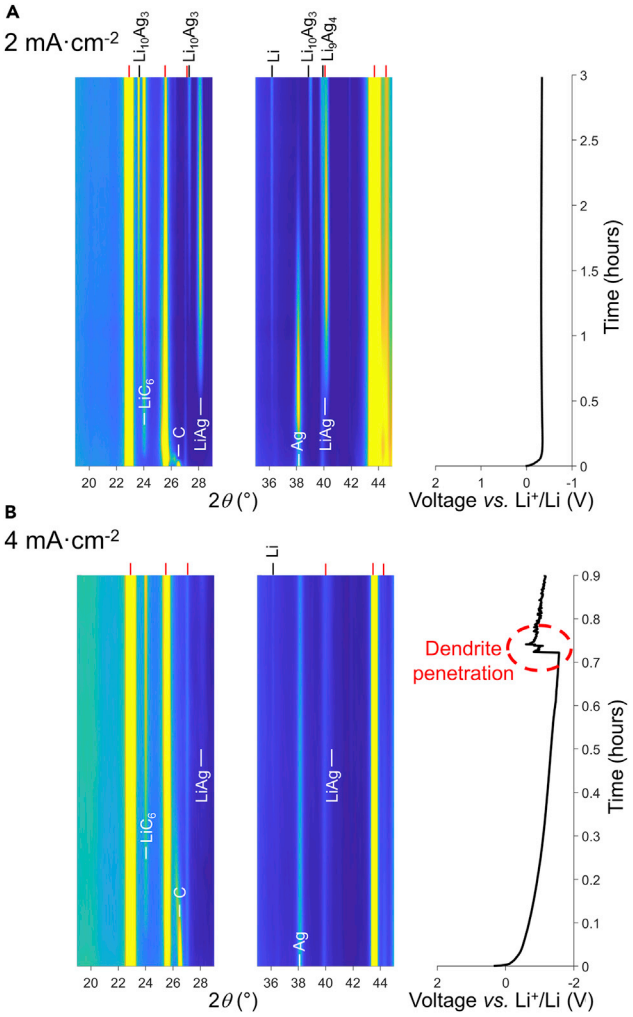

Figure 4. *Operando* powder X-ray diffraction color maps with corresponding electrochemistry

(A and B) Phase changes within the Ag-graphite composite layer during charge at 60°C at (A) 2 mA·cm^{-2} and (B) 4 mA·cm^{-2}. When charging at 4 mA·cm^{-2}, a sudden drop in cell potential to approximately 0 V is observed, indicating short circuit of the cell due to Li dendrite penetration of the solid electrolyte. Diffraction peaks corresponding to the cell body and Li_6PS_5Cl electrolyte are indicated with red marks.

on this understanding, we predict that carbon-based interlayers using carbons with higher Li diffusivity will enable higher rates of dendrite-free charge. It should be noted that these performances relate only to the anode and do not encompass the challenges of constructing a full all-solid-state anodeless battery with a composite cathode.[43,44]

Benefit of alloy interlayers

As Ag nanoparticles do not increase the critical current density for dendrite formation, what effect do they have on charging? Figure 6 shows a series of SEM images and associated EDX maps collected at the surface of the composite layer in contact with the current collector after passing 2 mA·h·cm^{-2} of charge at 0.1 mA·cm^{-2}, followed by careful removal of the current collector. Cross-sectional micrographs and EDX maps are also shown as Figure S4. The comparison is between two graphite layers that are identical, except that one contains Ag nanoparticles. In the absence

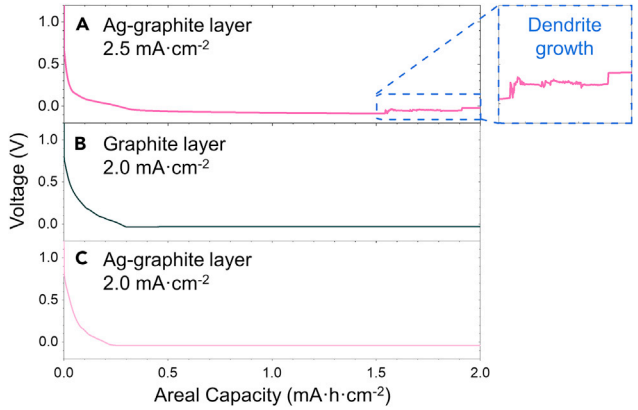

Figure 5. Voltage profiles showing charge of graphite and Ag-graphite composite layers, moving 2.0 mA·h·cm^{-2} capacity at 60°C

(A–C) (A) Charge of the Ag-graphite layer at 2.5 mA·cm^{-2} showing failure due to dendrite growth (magnified region); (B) charge of the graphite layer at 2.0 mA·cm^{-2} showing dendrite-free charge; and (C) charge of the silver-graphite layer at 2.0 mA·cm^{-2} showing dendrite-free charge.

of the Ag nanoparticles, on charging, Li metal forms in a highly heterogeneous (honeycomb) fashion above the graphite layer (i.e., between it and the current collector) (Figure 6B). In subsequent discharge, the Li metal remains above the graphite layer in the secondary electron images as well as in the black regions of the carbon EDX map (regions where carbon is not detected indicate the presence of low atomic number Li metal, Figure 6C). Compared with the corresponding data, in the presence of Ag nanoparticles, on charging, the region above the graphite layer (between it and the current collector) is more homogeneous and now contains Ag (Figure 6E). From the PXRD results in Figure 1, we ascribe the presence of Ag to the $Li_{10}Ag_3$ phase. From the SEM/EDX results in Figure S2B, collected at an earlier state of charge when the particles are just emerging form the interlayer, we know that Li metal is also formed (some of the particles show no detectable Ag in EDX). This is supported by PXRD from the end of charge showing the presence of Li (Figure S2A). Therefore, the layer in Figure 6E is composed of a combination of $Li_{10}Ag_3$ and Li. On subsequent discharge, much of the $Li_{10}Ag_3$ returns to the graphite layer. Although we cannot map Li directly by EDX, note that regions in the carbon EDX of the discharged sample devoid of carbon (the regions in black) are greater than the regions occupied by remaining Ag (Figure 6F). This suggests that some Li or an alloy that is highly Li-rich remains on the surface of the graphite layer. These results suggest that the main effect of Ag nanoparticles is that a layer of Li metal and $Li_{10}Ag_3$ alloy emerges relatively homogeneously from the graphite layer and then returns to the layer on discharge.

Returning to compare these findings with the recent work on other carbon-based composite layers, there are clear similarities in the way in which the carbon-based layers protect against dendrite growth by enabling Li-Ag alloy and Li metal deposition at the interface with the current collector, even though different types of carbon are used in the layer.[32] However, the type of carbon chosen will have a significant impact on the way in which Li is stored within the composite layer and the mechanism of Li transport through the layer on charge and discharge, and this will affect the rate performance.[45,46] It is anticipated that carbons that give high Li diffusivity through the composite layer will sustain higher rates of dendrite-free charge.

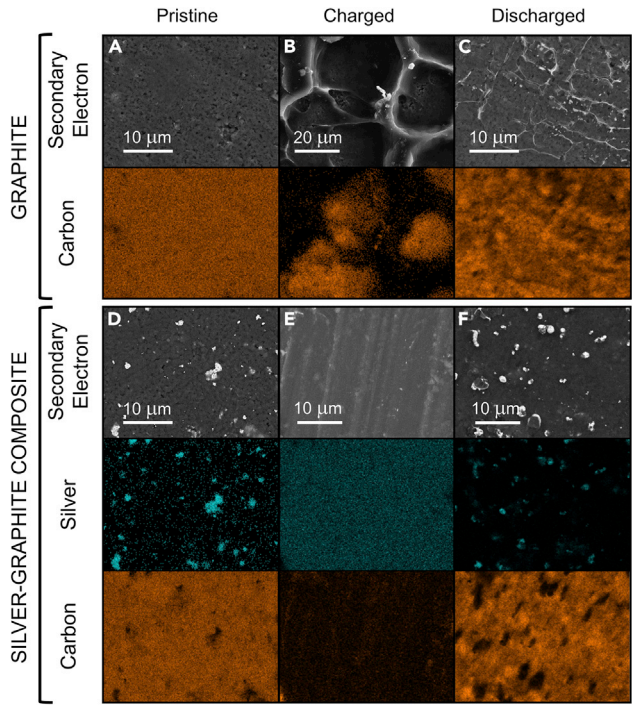

Figure 6. Scanning electron micrographs and energy dispersive X-ray spectroscopy color maps of graphite and Ag-graphite layer surfaces after removal of the current collector

(A–F) In (A–C), graphite only and in (D–F), Ag-graphite. Graphite (A) when pristine, (B) after charging, and (C) after discharging, showing the uneven deposition of Li against the current collector on charge, and Li remaining at the interlayer/current collector interface after discharge. Ag-graphite (D) when pristine, (E) after charging, and (F) after discharging, revealing homogeneous Li-Ag alloy formation at the interlayer/current collector following charge, and a return to a near-pristine state following discharge. The carbon energy dispersive X-ray spectroscopy color map is shown in orange and that of silver is shown in teal. Cells were cycled at 0.1 $mA \cdot cm^{-2}$ current density at 60°C, moving 2 $mA \cdot h \cdot cm^{-2}$ capacity. (A) and (C–F) scale bars are 10 μm, (B) scale bar is 20 μm.

Conclusions

The Ag-graphite composite interlayer anode functions at lower rates of charge by Li intercalation into graphite, followed by chemical reaction with Ag to form Li-rich Li-Ag alloy phases, as well as direct Li metal deposition at the current collector. At higher rates of charge, more Li metal formation is observed as the rate of electrochemical intercalation of Li into graphite exceeds the rate of chemical reaction. However, at rates ≥ 2.5 $mA \cdot cm^{-2}$, the rate of Li intercalation into the graphite-based interlayer is insufficient, and Li metal plates at the interface with the solid electrolyte, leading to dendrite growth and cell failure. For this reason, carbons with higher Li diffusivities will enable higher rates of dendrite-free charge. The Ag nanoparticles do not suppress Li dendrites any more than a graphite layer, but they do result in relatively homogeneous formation of $Li_{10}Ag_3$ and Li metal between the composite layer and the current collector of the anodeless cell, whereas in the absence of Ag, Li deposits heterogeneously between graphite and the current collector, and there is significant evidence of Li remaining after discharge.

EXPERIMENTAL PROCEDURES

Resource availability

Lead contact

Further information and requests for resources should be directed to and will be fulfilled by the lead contact, Peter Bruce (peter.bruce@materials.ox.ac.uk).

Materials availability

This study did not generate new unique materials.

Data and code availability

The data generated during this study have been deposited in the Oxford Research archive and is available at DOI: 10.5287/bodleian:kKBPZ282m.

Materials preparation

The Ag-graphite composite interlayer was prepared by spray deposition, using an in-house developed atomization and spray deposition instrument in an Ar-filled glovebox.[47,48] A solution of PVdF in a mixture of solvents (97% IPA, 3% NMP by volume) was prepared. Ag nanoparticles and graphite were suspended in this solution in a ratio of 1:3 by weight, then mixed and sonicated, giving a PVdF:Ag:graphite ratio the same as that described by Lee et al.[32] The suspension was atomized with compressed Ar gas, and spray-deposited onto a stainless-steel current collector which was heated at 110°C during the deposition to evaporate the solvent. This yielded a 10 × 10 cm^2 sheet of Ag-graphite composite interlayer composed of 22.5 wt % Ag nanoparticles, 67.5 wt % graphite and 10 wt % PVdF binder. Electrodes were cut from this sheet using a hollow punch, dried under vacuum at 70°C, and were uniaxially pressed against Li_6PS_5Cl powder (AMPCERA) under 400 MPa to make Li_6PS_5Cl disks with 5 μm (±1 μm) thick Ag-graphite composite layers adhered to one face. Li foils (50 μm thickness) were pressed onto the other face of the Li_6PS_5Cl disks to act as the counter electrode.

Standard LiC_x samples were prepared in coin cells with a graphite working electrode, Li foil counter electrode and 1 M $LiPF_6$ in EC/DMC (50:50 by volume) (Sigma Aldrich). Cells were charged at a rate of 10 $mA \cdot g^{-1}$, disassembled, washed in dry dimethyl carbonate (Sigma Aldrich), and dried under vacuum. The LiC_x phases were confirmed by PXRD. LiC_x samples were then mixed with Ag nanoparticles in a ratio of 6:1 by weight and were uniaxially pressed into pellets. The pellets were ground to powder in an agate pestle and mortar, and PXRD was performed.

Electrochemistry

Cycling was carried out using the Gamry 1010 E and Biologic VMP3 potentiostats. Low-rate cycling (30 $\mu A \cdot cm^{-2}$) was carried out at room temperature, whereas higher-rate cycling (2, 2.5 and 4 $mA \cdot cm^{-2}$) was carried out at 60°C. For higher-rate cycling, a 5 mm diameter Li metal counter electrode was used to minimize the contribution of voiding at the counter electrode interface to cell overpotential.[49–51] All cycling was carried out under a stack-pressure of 2 MPa. The capacity passed on charge was in excess of the capacity stored by Li intercalation into graphite in the composite layer (approx. 0.28 $mA \cdot h \cdot cm^{-2}$), and the maximum capacity stored by alloying with Ag (approx. 0.60 $mA \cdot h \cdot cm^{-2}$).

Powder X-ray diffraction

Operando PXRD, when cycling at the low rate of 30 $\mu A \cdot cm^2$, was carried out in reflection on a 3 kW Rigaku SmartLab diffractometer, using Cu Kα radiation. PXRD was carried out using a Rigaku cell with an Al-coated Be window which was protected with a 1 μm thick Cu current collector (GoodFellow), against which the Ag-graphite composite face of the cell was pressed. A conical spring was used to apply stack-pressure throughout cycling. A schematic showing the set-up is included as Figure S5.

A synchrotron X-ray source was used for higher rate cycling to achieve higher time resolution (Figure 4). Cell cycling was carried out on beamline I12 (JEEP) at the Diamond Light Source.[52] PXRD was carried out in transmission, with an X-ray spot-size

of 50 μm, in a custom-built tube cell.[3] Note that an X-ray energy of 56 keV was used, however two theta values have been converted to be comparable to data collected with Cu Kα radiation.

Ex situ PXRD was carried out on a Rigaku MiniFlex diffractometer, in a nitrogen atmosphere glovebox, using Cu Kα radiation. Samples were measured on low-background silicon sample holders.

Scanning electron microscopy and energy dispersive X-ray spectroscopy

Cells were disassembled in an Ar-filled glovebox, carefully removing the stainless-steel current collectors using a method that has previously been used in the literature.[53] Samples were mounted and transferred into the SEM (Zeiss Merlin) using an air-tight transfer device (Gatan). EDX was carried out using an X-max 150 silicon drift detector (Oxford Instruments) and analyzed using the Aztec software package.

SUPPLEMENTAL INFORMATION

Supplemental information can be found online at https://doi.org/10.1016/j.joule.2023.02.001.

ACKNOWLEDGMENTS

P.G.B. is indebted to the Faraday Institution (FIRG026), the Engineering and Physical Sciences Research Council (EP/M009521/1), and the Henry Royce Institute for Advanced Materials for financial support (EP/R00661X/1, EP/S019367/1, and EP/R010145/1). We thank Diamond Light Source, Didcot, United Kingdom for use of synchrotron radiation facilities and experimental support (experiment no. mg26082).

AUTHOR CONTRIBUTIONS

D.S.-J. and V.A. were involved in all aspects of the research. C.D. carried out spray deposition of interlayers, supervised by P.S.G. B.H., S.Z., and O.V.M. carried out synchrotron experiments at Diamond Light Source. D.L.R.M., H.G., and X.G. contributed to method development and data analysis. R.A.H. performed and analyzed *operando* PXRD experiments. The project was managed by P.A. and supervised by P.G.B. P.G.B. wrote the manuscript with contributions from D.S.-J. and V.A.

DECLARATION OF INTERESTS

The authors declare no competing interests.

Received: August 22, 2022
Revised: October 13, 2022
Accepted: January 31, 2023
Published: February 24, 2023

REFERENCES

1. Janek, J., and Zeier, W.G. (2016). A solid future for battery development. Nat. Energy *1*, 16141. https://doi.org/10.1038/nenergy.2016.141.

2. Pasta, M., Armstrong, D., Brown, Z.L., Bu, J., Castell, M.R., Chen, P., Cocks, A., Corr, S.A., Cussen, E.J., Darnbrough, E., et al. (2020). 2020 roadmap on solid-state batteries. J. Phys. Energy *2*, 032008. https://doi.org/10.1088/2515-7655/ab95f4.

3. Ning, Z., Jolly, D.S., Li, G., De Meyere, R., Pu, S.D., Chen, Y., Kasemchainan, J., Ihli, J., Gong, C., Liu, B., et al. (2021). Visualizing plating-induced cracking in lithium-anode solid-electrolyte cells. Nat. Mater. *20*, 1121–1129. https://doi.org/10.1038/s41563-021-00967-8.

4. Porz, L., Swamy, T., Sheldon, B.W., Rettenwander, D., Frömling, T., Thaman, H.L., Berendts, S., Uecker, R., Carter, W.C., and Chiang, Y.M. (2017). Mechanism of lithium metal penetration through inorganic solid electrolytes. Adv. Energy Mater. *7*, 1–12. https://doi.org/10.1002/aenm.201701003.

5. Kazyak, E., Wang, M.J., Lee, K., Yadavalli, S., Sanchez, A.J., Thouless, M.D., Sakamoto, J., and Dasgupta, N.P. (2022). Understanding the electro-chemo-mechanics of Li plating in anode-free solid-state batteries with operando 3D microscopy. Matter *5*, 3912–3934. https://doi.org/10.1016/j.matt.2022.07.020.

6. Raj, V., Venturi, V., Kankanallu, V.R., Kuiri, B., Viswanathan, V., and Aetukuri, N.P.B. (2022). Direct correlation between void formation and lithium dendrite growth in solid-state electrolytes with interlayers. Nat. Mater. *21*, 1050–1056. https://doi.org/10.1038/s41563-022-01264-8.

7. Oh, P., Yun, J., Choi, J.H., Saqib, K.S., Embleton, T.J., Park, S., Lee, C., Ali, J., Ko, K., and Cho, J. (2022). Development of high-energy anodes for all-solid-state lithium batteries based on sulfide electrolytes. Angew. Chem. Int. Ed. Engl. *61*, e202201249. https://doi.org/10.1002/anie.202201249.

8. Kim, S.Y., and Li, J. (2021). Porous mixed ionic electronic conductor interlayers for solid-state batteries. Energy Mater. Adv. *2021*, 1–15. https://doi.org/10.34133/2021/1519569.

9. Krauskopf, T., Richter, F.H., Zeier, W.G., and Janek, J. (2020). Physicochemical concepts of the lithium metal anode in solid-state batteries. Chem. Rev. *120*, 7745–7794. https://doi.org/10.1021/acs.chemrev.0c00431.

10. Wang, T., Duan, J., Zhang, B., Luo, W., Ji, X., Xu, H., Huang, Y., Huang, L., Song, Z., Wen, J., et al. (2022). A self-regulated gradient interphase for dendrite-free solid-state Li batteries. Energy Environ. Sci. *15*, 1325–1333. https://doi.org/10.1039/D1EE03604A.

11. Kim, S., Jung, C., Kim, H., Thomas-Alyea, K.E., Yoon, G., Kim, B., Badding, M.E., Song, Z., Chang, J.M., Kim, J., et al. (2020). The role of interlayer chemistry in Li-metal growth through a garnet-type solid electrolyte. Adv. Energy Mater. *10*, 1903993. https://doi.org/10.1002/aenm.201903993.

12. Taylor, N.J., Stangeland-Molo, S., Haslam, C.G., Sharafi, A., Thompson, T., Wang, M., Garcia-Mendez, R., and Sakamoto, J. (2018). Demonstration of high current densities and extended cycling in the garnet $Li_7La_3Zr_2O_{12}$ solid electrolyte. J. Power Sources *396*, 314–318. https://doi.org/10.1016/j.jpowsour.2018.06.055.

13. Feng, W., Dong, X., Li, P., Wang, Y., and Xia, Y. (2019). Interfacial modification of Li/Garnet electrolyte by a lithiophilic and breathing interlayer. J. Power Sources *419*, 91–98. https://doi.org/10.1016/j.jpowsour.2019.02.066.

14. He, M., Cui, Z., Chen, C., Li, Y., and Guo, X. (2018). Formation of self-limited, stable and conductive interfaces between garnet electrolytes and lithium anodes for reversible lithium cycling in solid-state batteries. J. Mater. Chem. A *6*, 11463–11470. https://doi.org/10.1039/C8TA02276C.

15. Wakasugi, J., Munakata, H., and Kanamura, K. (2017). Effect of gold layer on interface resistance between lithium metal anode and $Li_{6.25}Al_{0.25}La_3Zr_2O_{12}$ solid electrolyte. J. Electrochem. Soc. *164*, A1022–A1025. https://doi.org/10.1149/2.0471706jes.

16. Tsai, C.L., Roddatis, V., Chandran, C.V., Ma, Q., Uhlenbruck, S., Bram, M., Heitjans, P., and Guillon, O. (2016). $Li_7La_3Zr_2O_{12}$ interface modification for Li dendrite prevention. ACS Appl. Mater. Interfaces *8*, 10617–10626. https://doi.org/10.1021/acsami.6b00831.

17. Dubey, R., Sastre, J., Cancellieri, C., Okur, F., Forster, A., Pompizii, L., Priebe, A., Romanyuk, Y.E., Jeurgens, L.P.H., Kovalenko, M.V., and Kravchyk, K.V. (2021). Building a better Li-garnet solid electrolyte/metallic Li interface with antimony. Adv. Energy Mater. *11*, 2102086. https://doi.org/10.1002/aenm.202102086.

18. Fu, K.K., Gong, Y., Fu, Z., Xie, H., Yao, Y., Liu, B., Carter, M., Wachsman, E., and Hu, L. (2017). Transient behavior of the metal interface in lithium metal–garnet batteries. Angew. Chem. Int. Ed. Engl. *56*, 14942–14947. https://doi.org/10.1002/anie.201708637.

19. Lu, Y., Huang, X., Ruan, Y., Wang, Q., Kun, R., Yang, J., and Wen, Z. (2018). An in situ element permeation constructed high endurance Li-LLZO interface at high current densities. J. Mater. Chem. A *6*, 18853–18858. https://doi.org/10.1039/C8TA07241H.

20. Luo, W., Gong, Y., Zhu, Y., Fu, K.K., Dai, J., Lacey, S.D., Wang, C., Liu, B., Han, X., Mo, Y., et al. (2016). Transition from Superlithiophobicity to Superlithiophilicity of garnet solid-state electrolyte. J. Am. Chem. Soc. *138*, 12258–12262. https://doi.org/10.1021/jacs.6b06777.

21. Zhao, N., Fang, R., He, M.H., Chen, C., Li, Y.Q., Bi, Z.J., and Guo, X.X. (2018). Cycle stability of lithium/garnet/lithium cells with different intermediate layers. Rare Met. *37*, 473–479. https://doi.org/10.1007/s12598-018-1057-3.

22. Luo, W., Gong, Y., Zhu, Y., Li, Y., Yao, Y., Zhang, Y., Fu, K.K., Pastel, G., Lin, C.-F., Mo, Y., et al. (2017). Reducing interfacial resistance between garnet-structured solid-state electrolyte and Li-metal anode by a germanium layer. Adv. Mater. *29*, 1–7. https://doi.org/10.1002/adma.201606042.

23. Han, S.Y., Lee, C., Lewis, J.A., Yeh, D., Liu, Y., Lee, H., and Mcdowell, M.T. (2021). Stress evolution during cycling of alloy-anode solid-state batteries. Joule *5*, 2450–2465. https://doi.org/10.1016/j.joule.2021.07.002.

24. Obrovac, M.N., and Chevrier, V.L. (2014). Alloy negative electrodes for Li-ion batteries. Chem. Rev. *114*, 11444–11502. https://doi.org/10.1021/cr500207g.

25. Lewis, J.A., Cavallaro, K.A., Liu, Y., and McDowell, M.T. (2022). The promise of alloy anodes for solid-state batteries. Joule *6*, 1418–1430. https://doi.org/10.1016/j.joule.2022.05.016.

26. Schweidler, S., De Biasi, L., Schiele, A., Hartmann, P., Brezesinski, T., and Janek, J. (2018). Volume changes of graphite anodes revisited: a combined operando X-ray diffraction and in situ pressure analysis study. J. Phys. Chem. C *122*, 8829–8835. https://doi.org/10.1021/acs.jpcc.8b01873.

27. Xing, X., Li, Y., Wang, S., Liu, H., Wu, Z., Yu, S., Holoubek, J., Zhou, H., and Liu, P. (2021). Graphite-based lithium-free 3D hybrid anodes for high energy density all-solid-state batteries. ACS Energy Lett. *6*, 1831–1838. https://doi.org/10.1021/acsenergylett.1c00627.

28. Takada, K., Inada, T., Kajiyama, A., Sasaki, H., Kondo, S., Watanabe, M., Murayama, M., and Kanno, R. (2003). Solid-state lithium battery with graphite anode. Solid State Ionics *158*, 269–274. https://doi.org/10.1016/S0167-2738(02)00823-8.

29. Ye, L., and Li, X. (2021). A dynamic stability design strategy for lithium metal solid state batteries. Nature *593*, 218–222. https://doi.org/10.1038/s41586-021-03486-3.

30. Futscher, M.H., Amelal, T., Sastre, J., Müller, A., Patidar, J., Aribia, A., Thorwarth, K., Siol, S., and Romanyuk, Y.E. (2022). Influence of amorphous carbon interlayers on nucleation and early growth of lithium metal at the current collector-solid electrolyte interface. J. Mater. Chem. A Mater. *10*, 15535–15542. https://doi.org/10.1039/d2ta02843c.

31. Xie, H., Yang, C., Ren, Y., Xu, S., Hamann, T.R., Mcowen, D.W., Wachsman, E.D., and Hu, L. (2021). Amorphous-carbon-coated 3D solid electrolyte for an electro-chemomechanically stable lithium metal anode in solid-state batteries. Nano Lett. *21*, 6163–6170. https://doi.org/10.1021/acs.nanolett.1c01748.

32. Lee, Y.G., Fujiki, S., Jung, C., Suzuki, N., Yashiro, N., Omoda, R., Ko, D.S., Shiratsuchi, T., Sugimoto, T., Ryu, S., et al. (2020). High-energy long-cycling all-solid-state lithium metal batteries enabled by silver–carbon composite anodes. Nat. Energy *5*, 299–308. https://doi.org/10.1038/s41560-020-0575-z.

33. Zhou, L., Park, K.-H., Sun, X., Lalère, F., Adermann, T., Hartmann, P., and Nazar, L.F. (2019). Solvent-engineered design of argyrodite Li_6PS_5X (X = Cl, Br, I) solid electrolytes with high ionic conductivity. ACS Energy Lett. *4*, 265–270. https://doi.org/10.1021/acsenergylett.8b01997.

34. Yu, C., van Eijck, L., Ganapathy, S., and Wagemaker, M. (2016). Synthesis, structure and electrochemical performance of the argyrodite Li_6PS_5Cl solid electrolyte for Li-ion solid state batteries. Electrochim. Acta *215*, 93–99. https://doi.org/10.1016/j.electacta.2016.08.081.

35. Höltschi, L., Borca, C.N., Huthwelker, T., Marone, F., Schlepütz, C.M., Pelé, V., Jordy, C., Villevieille, C., Kazzi, M.E. El, and Novák, P. (2021). Performance-limiting factors of graphite in sulfide-based all-solid-state lithium-ion batteries. Electrochim. Acta *389*, 138735. https://doi.org/10.1016/j.electacta.2021.138735.

36. Banerjee, A., Wang, X., Fang, C., Wu, E.A., and Meng, Y.S. (2020). Interfaces and interphases in all-solid-state batteries with inorganic solid electrolytes. Chem. Rev. *120*, 6878–6933. https://doi.org/10.1021/acs.chemrev.0c00101.

37. Freeth, W.E., and Raynor, G.V. (1953). The constitution of the system silver-lithium. J. Inst. Metals *82*, 569–574.

38. Dahn, J.R. (1991). Phase diagram of LixC6. Phys. Rev. B Condens. Matter *44*, 9170–9177. https://doi.org/10.1103/PhysRevB.44.9170.

39. Missyul, A., Bolshakov, I., and Shpanchenko, R. (2017). XRD study of phase transformations in lithiated graphite anodes by Rietveld method. Powder Diffr. *32*, S56–S62. https://doi.org/10.1017/S0885715617000458.

40. Taillades, G., and Sarradin, J. (2004). Silver: high performance anode for thin film lithium ion batteries. J. Power Sources *125*, 199–205. https://doi.org/10.1016/j.jpowsour.2003.07.004.

41. Pavlyuk, V.V., Dmytriv, G.S., Tarasiuk, I.I., Chumak, I.V., Pauly, H., and Ehrenberg, H. (2010). Polymorphism of LiAg. Solid State Sci. *12*, 274–280. https://doi.org/10.1016/j.solidstatesciences.2009.11.006.

42. Suzuki, N., Yashiro, N., Fujiki, S., Omoda, R., Shiratsuchi, T., Watanabe, T., and Aihara, Y. (2021). Highly cyclable all-solid-state battery with deposition-type lithium metal anode based on thin carbon black layer. Adv. Energy Sustain. Res. *2*, 2100066. https://doi.org/10.1002/aesr.202100066.

43. Minnmann, P., Strauss, F., Bielefeld, A., Ruess, R., Adelhelm, P., Burkhardt, S., Dreyer, S.L., Trevisanello, E., Ehrenberg, H., Brezesinski, T., et al. (2022). Designing cathodes and cathode active materials for solid-state batteries. Adv. Energy Mater. *12*. https://doi.org/10.1002/aenm.202201425.

44. Gao, X., Liu, B., Hu, B., Ning, Z., Spencer Jolly, D., Zhang, S., Perera, J., Bu, J., Liu, J., Doerrer, C., et al. (2022). Solid-state lithium battery cathodes operating at low pressures. Joule *6*, 636–646. https://doi.org/10.1016/j.joule.2022.02.008.

45. Kaskhedikar, N.A., and Maier, J. (2009). Lithium storage in carbon nanostructures. Adv. Mater. *21*, 2664–2680. https://doi.org/10.1002/adma.200901079.

46. Persson, K., Sethuraman, V.A., Hardwick, L.J., Hinuma, Y., Meng, Y.S., Van Der Ven, A., Srinivasan, V., Kostecki, R., and Ceder, G. (2010). Lithium diffusion in graphitic carbon. J. Phys. Chem. Lett. *1*, 1176–1180. https://doi.org/10.1021/jz100188d.

47. Huang, C., Grobert, N., Watt, A.A.R., Johnston, C., Crossley, A., Young, N.P., and Grant, P.S. (2013). Layer-by-layer spray deposition and unzipping of single-wall carbon nanotube-based thin film electrodes for electrochemical capacitors. Carbon *61*, 525–536. https://doi.org/10.1016/j.carbon.2013.04.107.

48. Huang, C., Young, N.P., Zhang, J., Snaith, H.J., and Grant, P.S. (2017). A two layer electrode structure for improved Li Ion diffusion and volumetric capacity in Li Ion batteries. Nano Energy *31*, 377–385. https://doi.org/10.1016/j.nanoen.2016.11.043.

49. Kasemchainan, J., Zekoll, S., Spencer Jolly, D., Ning, Z., Hartley, G.O., Marrow, J., and Bruce, P.G. (2019). Critical stripping current leads to dendrite formation on plating in lithium anode solid electrolyte cells. Nat. Mater. *18*, 1105–1111. https://doi.org/10.1038/s41563-019-0438-9.

50. Spencer Jolly, D., Ning, Z., Darnbrough, J.E., Kasemchainan, J., Hartley, G.O., Adamson, P., Armstrong, D.E.J., Marrow, J., and Bruce, P.G. (2020). Sodium/Na β″ alumina interface: effect of pressure on voids. ACS Appl. Mater. Interfaces *12*, 678–685. https://doi.org/10.1021/acsami.9b17786.

51. Seymour, I.D., and Aguadero, A. (2021). Suppressing void formation in all-solid-state batteries: the role of interfacial adhesion on alkali metal vacancy transport. J. Mater. Chem. A *9*, 19901–19913. https://doi.org/10.1039/D1TA03254B.

52. Drakopoulos, M., Connolley, T., Reinhard, C., Atwood, R., Magdysyuk, O., Vo, N., Hart, M., Connor, L., Humphreys, B., Howell, G., et al. (2015). I12: the Joint Engineering, Environment and processing (JEEP) beamline at Diamond Light Source. J. Synchrotron Radiat. *22*, 828–838. https://doi.org/10.1107/S1600577515003513.

53. Wang, M.J., Carmona, E., Gupta, A., Albertus, P., and Sakamoto, J. (2020). Enabling "lithium-free" manufacturing of pure lithium metal solid-state batteries through in situ plating. Nat. Commun. *11*, 5201. https://doi.org/10.1038/s41467-020-19004-4.